Measurement of the Local Intrinsic Curvature of a $l = 1$ Radio-Vortex at 30 GHz

Lorenzo Scalcinati[1], Bruno Paroli[1, *], Mario Zannoni[2], and Marco A. C. Potenza[1]

Abstract—We exploit the properties of differential geometry of minimal surfaces to introduce a novel approach for characterizing wavefronts. Since Gaussian and mean curvatures describe global and local properties of any differentiable surface, a method for characterizing wavefronts endowed with non-trivial topological features has been introduced. We provide experimental evidence that the wavefront of an $l = 1$ radio-vortex at 30 GHz can be fully characterized by exploiting the wavefront phase in the far field of the source, accessing a small portion of the beam only. A particular care is dedicated to distinguish diffraction effects from the intrinsic curvature of the helicoidal wavefront. Results are applicable to the local measurement of the topological charge and to the local detection of orbital angular momentum radiation at the millimetric wavelengths.

1. INTRODUCTION

Electromagnetic vortices and singular wavefronts are recently attracting increasing interest in view of scientific and technological applications. From a classical point of view, radiation endowed with Orbital Angular Momentum (OAM) is characterized by helical wavefronts, where the topological charge is the winding number [1–3]. Relevant results have been obtained in the field of singular optics, with potential applications to telecommunication systems. Several results obtained with singular optics have also been recently reproduced by simply scaling at the millimeter wave range [4, 5]. Beyond the fundamental interest and the different diagnostic approach achievable with electromagnetic waves, which allow for a direct measure of the field, millimeter waves allow for huge advantages with respect to visible/IR light when propagating through turbulent media [6, 7]. Indeed, the effects of scintillation due to fog and air turbulence make the optical systems even ineffective, while millimetric waves in proper bands are almost undisturbed. On the contrary, large wavelengths undergo a strong limitation when the waves propagate over long distances. Diffraction is more effective, imposing a beam divergence $\theta \approx \lambda/D$ for a transmitting antenna with transverse size D at a given the wavelength λ. Similarly, the far field regime is reached much closer to the source, namely at a distance $z \sim \frac{D^2}{\lambda}$. As a result, working in the far field with a diverging beam is almost mandatory when considering millimetric waves. Unfortunately, this is in contrast with the traditional approaches to measure vortices, which typically require to access the entire wavefront or at least a relevant part of it.

Recently, the feasibility of local measurements of the topological charge has been proven in the visible wavelength range by adopting a proper scanning interferometry (asymmetric lateral coherence, see [8–10]). It has been possible by exploiting the geometrical differential properties of a helical wavefront curvature [11–13]. More precisely, it has been proven that the wavefront curvature due to the beam divergence C_D in the far field can be said apart from the intrinsic local curvature C_I of the helicoidal wavefront, proportional to the topological charge of the vortex. Both are related to the differential

[1] Dipartimento di Fisica, Universitá degli Studi di Milano, via G. Celoria, 16, 20133 Milano, Italy. [2] Physics Department, University of Milano Bicocca, 20126, Piazza della Scienza 3, Milano, Italy.

geometry of the wavefront, but they are basically different: they exhibit opposite Gaussian curvatures when being measured along the principal directions, i.e., the directions of maximum and minimum curvature. Therefore, just the Gaussian curvatures deliver fundamental differences in the geometrical properties of the radiation wavefront.

In this paper we report the first experimental evidence of the curvature properties of a $l = 1$ radio-vortex at the millimeter wavelengths (30 GHz) through the measurement of the Gaussian curvature introduced above and the mean curvature that defines the main behavior of the minimal surfaces such as the helicoid [14, 15]. This extends the applicability of the local method developed for optical vortices to millimetric waves, paving the way to a novel framework of measuring the phase properties of wavefronts.

The paper is organized as follows. We describe the theoretical framework in Section 2. The experimental setup and measurement method are shown in Section 3. Section 4 is devoted to results and discussions. Finally, we present conclusions in Section 5.

2. THEORETICAL FORMULATION

Let's consider a reference frame x, y, z where x is the horizontal coordinate, y the vertical coordinate, and z the propagation axis of the radiation beam. By assuming a Gaussian beam with a screw phase dislocation, the phase term depending on the curvatures C_D and C_I is

$$\phi(x) = \frac{kx^2}{2R(z)} + l\theta \,,$$

where $k = 2\pi/\lambda$, λ is the wavelength, $R(z)$ the curvature radius of the Gaussian beam, l the topological charge, and θ the azimuthal angle measured on a detection plane orthogonal to the propagation axis (see Fig. 2(a)). By expressing θ as a function of x, we find

$$\phi(x) = \frac{kx^2}{2R(z)} + l \arccos \frac{x}{\sqrt{x^2 + y_0^2}} \,, \tag{1}$$

where $\phi(x)$ is defined along a horizontal linear path at a vertical position y_0 from the singularity.

The curvature along the x coordinate is obtained from the second derivative of $\phi(x)$ as (see [16])

$$C(x) = \frac{1}{k}\frac{d^2\phi(x)}{dx^2} = 1/R(z) + l\frac{2xy_0}{(x^2 + y_0^2)^2\,k} = C_D + C_I. \tag{2}$$

Equation (2) shows that the curvature is the sum of C_D and C_I as a consequence of the linearity of the derivative operator.

Since $C_I(x) = C(x) - C_D(x)$ the Gaussian curvature $K_h = C_{I,\text{max}}C_{I,\text{min}}$ and mean curvature $H_h = 1/2(C_{I,\text{max}} + C_{I,\text{min}})$ as a function of the phase functions $\phi(x)$, $\phi_G(x)$ are written as

$$K_h = \max\left[\frac{1}{k}\frac{d^2}{dx^2}(\phi(x) - \phi_G(x))\right] \min\left[\frac{1}{k}\frac{d^2}{dx^2}(\phi(x) - \phi_G(x))\right] \tag{3}$$

and

$$H_h = \frac{1}{2}\left\{\max\left[\frac{1}{k}\frac{d^2}{dx^2}(\phi(x) - \phi_G(x))\right] + \min\left[\frac{1}{k}\frac{d^2}{dx^2}(\phi(x) - \phi_G(x))\right]\right\} \,, \tag{4}$$

where $\phi_G(x)$ is the phase of the transmitted Gaussian beam ($l = 0$) observed at the detection plane and $d^2\phi_G(x)/dx^2 = k\,C_D$.

Equations (3) and (4) show that the Gaussian and mean curvatures are obtained from $\phi(x)$ and $\phi_G(x)$ measured along linear paths. Both quantities are experimentally accessible.

3. EXPERIMENTAL SETUP

A radio-vortex beam with topological charge $l = 1$ is generated by means of a Spiral Phase Plate (SPP, see Fig. 1), 170 mm in diameter, designed to operate at a frequency of 30 GHz. It has been realized

Figure 1. Picture of the SPP used to generate the radio-vortex.

in Polytetrafluoroethylene (PTFE) at mill. To be properly shaped at the machines, two halves have been worked separately, then kept in position by an external polymethylmethacrylate annular frame of 170 mm internal diameter (see Fig. 1).

The experimental setup is shown in Fig. 2. Two WR-28 FLANN standard pyramidal gain horns, 20 dB gain, are used as transmitter and receiver. The SPP is positioned 245 mm far from the transmitter. The beam intensity outside the SPP is less than 0.1% of the total emitted power. The receiver is in the far field of the beam, 248 mm from the SPP, in order to operate in the far field and to access the whole beam intensity profile.
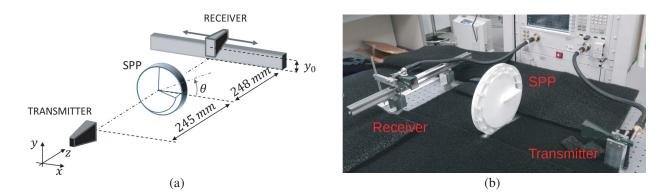

Figure 2. (a) Geometry of the experimental setup. The scan has been performed in the horizontal x direction through a linear translation stage positioned at two different vertical positions from the singularity. (b) Picture of the experimental setup.

The experimental setup is mounted on an optical bench shielded with flat RF absorbers (ECCOSORB®HR-10) as shown in Fig. 2(b). The field is generated and acquired by means of an Agilent Technologies PNA-X Vector Network Analyzer (VNA) connected to the antennas through ultra-flexible GORE RF coaxial cables. The covered frequency range is 29.9–30.1 GHz in 101 points. The IF width is 1 kHz. The scattering parameters of the radiation field are measured at different positions along the x coordinate by translating the receiver over a linear path 180 mm long. Scans are performed with 5 mm sampling distance and 1 mm accuracy at vertical distances $y_0 = 0$ mm and $y_0 = 35$ mm from the singularity.

4. RESULTS AND DISCUSSION

The intensity and phase profiles of the radio-vortex are obtained from the scattering parameter $S_{21} = |S_{21}|e^{i\phi}$, where $|S_{21}|(dB) = 10 \log_{10}(P_2/P_1)$. Here P_1 is the total emitted power, while P_2 is the nominal power measured at the exit of the SPP. P_2 is proportional to the radiation intensity measured at the exit of the SPP, $I \propto P_2$. Unavoidable misalignments in the transversal and angular positions between the transmitter, SPP, and receiver produce an uncertainty in the position of the singularity about 5 mm at the detection plane. In comparison, the precision obtained by assessing the horizontal position from the measured intensity profiles shown in Fig. 3 is higher. The minima of the fit functions correspond to the horizontal position of the singularity in the detection plane. Starting from Fig. 4 the position $x = 0$ (on-axis) is identified by means of the intensity profiles reported in Fig. 3. All the *right* plots show fewer points with respect to the *left* ones because the probe scans a chord of the SPP.
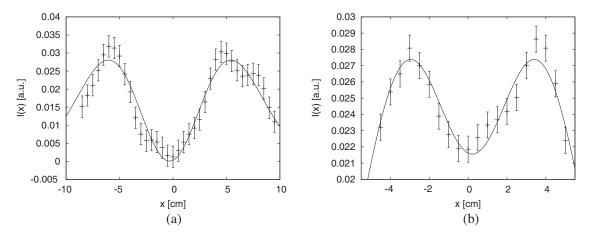

Figure 3. Intensity profiles of the Gaussian beam with screw phase dislocation on axis ((a) $y = 0$) and at $y_0 = 35$ mm from the singularity (b). Black solid line indicates the theoretical fit of a $l = 1$ Laguerre-Gauss mode. Error bars are the statistical errors extracted from the theoretical fits.
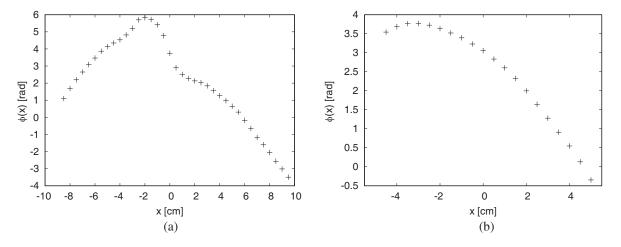

Figure 4. Phase profiles of the radiation beam with screw phase dislocation ($l = 1$) generated with the SPP and measured on axis ((a) $y = 0$) and at $y_0 = 35$ mm from the singularity (b).

Results are compared to the theoretical fit:

$$I(x) = I_0 \left[(x - s)^2 + y_0^2\right] \exp\left\{\frac{-2[(x - s)^2 + y_0^2]}{w^2}\right\} , \tag{5}$$

where the position of the singularity s, amplitude I_0, and beam size w are free parameters. Eq. (5) is the intensity of the $l = 1$ Laguerre-Gauss mode

$$
\begin{aligned}
E(r,\theta,z,t;k) \; = \; & A(r,z) \; \exp[i(2p+|l|+1)\psi(z)] \\
& \exp\left[\frac{-ikr^2}{2R(z)}\right] \exp[i(kz-\omega t)]\exp(il\theta) \,,
\end{aligned}
\tag{6}
$$

where r is the radial coordinate in a plane perpendicular to the propagation axis z, t the time, $\psi(z)$ the Gouy phase shift, and $A(r,z)$ is:

$$
A(r,z) = E_0 \left(\frac{\sqrt{2}r}{w(z)}\right)^{|l|} L_p^{|l|}\left(\frac{2r^2}{w(z)^2}\right) \frac{w_0}{w(z)} \exp\left[\frac{-r^2}{w(z)^2}\right] \,,
\tag{7}
$$

where $L_p^{|l|}$ are the generalized Laguerre polynomials; p is the number of nodes in the radial direction; $w(z)$ is the Gaussian beam size; and $w_0 = w(0)$. In our case $p = 0$ and $l = 1$ thus $L_p^{|l|}\left(\frac{2r^2}{w(z)^2}\right) = 1$. From $I = EE^*$ we find

$$
I = I_0 \, r^2 \exp\left(\frac{-2r^2}{w^2}\right) \,,
\tag{8}
$$

where $I_0 = 2E_0^2 w_0^2/w^4$. By posing $r = (x-s)^2 + y_0^2$ in Eq. (8), we obtain Eq. (5).

The phase profiles $\phi(x)$ measured on axis and at $35\,\text{mm}$ from the singularity are shown in Fig. 4. Notice that the intensity profile on axis evidences a fast phase change when passing the singularity. This effect is not observed at $y_0 = 35\,\text{mm}$ because of the smooth phase variation of the arccos (see Eq. (1)) by increasing y_0. The combined effect of C_D and C_I produces asymmetric profiles. To distinguish C_D and C_I the SPP was removed, and $\phi_G(x)$ was measured on the detection plane. The model has then been fitted to data assuming the far field approximation:

$$
\phi_G(x) = \left(\sqrt{(x-s)^2 + y_0^2 + z_0^2} - z_0\right)k + c_1 \,,
\tag{9}
$$

where c_1 is an arbitrary additive constant, and z_0 is the distance between the transmitter and the receiver. Data and fits are shown in Fig. 5.
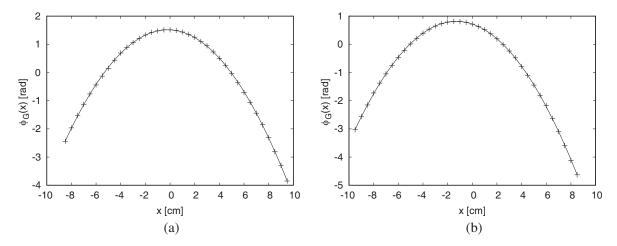

Figure 5. Phase profiles of the radiation beam on axis ((a) $y = 0$) and at $y_0 = 35\,\text{mm}$ from the propagation axis (b) measured after removing the SPP. Black solid lines are the curves fitted to data.

By using the datasets $\phi(x)$ in Fig. 4 and the fit functions $\phi_G(x)$ in Fig. 5, we find the phase differences $\phi_{LG} = \phi - \phi_G$ as shown Fig. 6.

The considerable deviations of data with respect to the theoretical fit obtained for the on axis profile (Fig. 6(a)) are due to the low intensity close to the singularity that reduces the signal-to-noise-ratio of
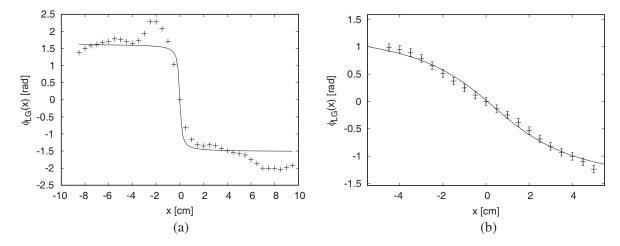
(a)

(b)

Figure 6. Phase profiles of the phase difference $\phi_{LG} = \phi - \phi_G$ on axis ((a) $y = 0$) and at $y_0 = 35\,\text{mm}$ from the singularity (b). Here ϕ is the dataset in Fig. 4 and ϕ_G is the best fit in Fig. 5. Black solid lines are the curves fitted to data.
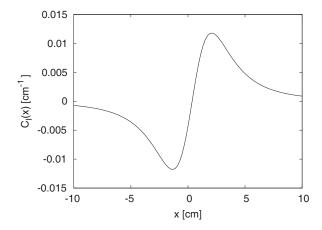

Figure 7. Transverse curvature of the helicoidal wavefront $C_I(x)$ calculated from the fit function of data in Fig. 6(b).

the measurements. Nevertheless, data qualitatively show the expected step-like function (see Eq. (1)). This function becomes smoother by increasing the vertical distance from the singularity, as it occurs for $y_0 = 35\,\text{mm}$ (Fig. 6(b)). Notice that the theoretical arccos function of the fit (the second term in Eq. (1)) closely follows the experimental data. The statistical error is 0.07 rad.

We show in Fig. 7 the intrinsic curvature $C_I = (1/k)[d^2(\phi(x) - \phi_G)/dx^2]$ of the helicoidal wavefront obtained by deriving the fit function ϕ_{LG} in Fig. 6(b) ($y_0 = 35\,\text{mm}$).

From this result we obtain the Gaussian curvature $K_h = C_{I,\text{max}}\, C_{I,min} = -1.4\,\text{m}^{-2}$ which is in agreement with the value obtained from pure geometrical considerations $K_g = -c_h^2/(c_h^2 + \rho_h^2)^2 = -1.1 \pm 0.4\,\text{m}^{-2}$, where $c_h = 1/k$ is the helicoid slant and p_h the radial distance from the singularity with 5 mm uncertainty. Notice that the Gaussian curvature is a negative, unique characteristic of the OAM beams, at variance to traditional radiation.

The mean curvature H_h has been obtained from data shown in Fig. 4 with two local fits (11 data points) around $x_1 = -25\,\text{mm}$ and $x_2 = 25\,\text{mm}$ and then deriving the two independent fits to obtain the relative curvatures $C_{I,1}(x)$ and $C_{I,2}(x)$. The average between the maximum curvature $\max[C_{I,2}(x)] = 0.0146\,\text{cm}^{-1}$ and the minimum curvature $\min[C_{I,1}(x)] = -0.0154\,\text{cm}^{-1}$ gives $H_h = -4$ $10^{-4}\,\text{cm}^{-1}$. It shows a value close to zero as predicted by the theory of the minimal surfaces [17].

The topological charge can be measured in a local manner from the curvature $C_I(x)$ deduced

from transverse measurements of the phase functions, being $l = k\, C_I(x^2 + y_0^2)^2/(2xy_0)$. To this aim measurements can also be performed far from the singularity, but the position of the singularity from the scan path should be known. Both the radio-vortex and the pure Gaussian beam are necessary to measure $\phi(x)$ and $\phi_G(x)$, respectively, and they should be imposed at the source level (by inserting and removing the SPP in our case). However, at large distances $\phi_G(x)$ becomes almost linear, and the pure Gaussian beam ($l = 0$) is in principle not strictly necessary, with the corresponding curvature being negligible.

5. CONCLUSIONS

Stemming from results recently obtained in the visible spectrum with lasers, we have introduced a formalism and the corresponding experimental technique based on a scan interferometric method to measure the Gaussian and mean curvatures of wavefronts endowed with non-trivial topological properties. The wavefront of a radio-vortex has been characterized in the far field of the source, thus proving the feasibility of local measurements of the topological charge. The two curvatures are obtained by separating the helical wavefront from the phase profile of the Gaussian beam undergoing diffraction. To the best of our knowledge, this is the first time a radio-vortex curvature is characterized in the far filed of the source.

The Gaussian and mean curvatures are compatible with the theoretical expectations based on geometrical/diffraction arguments. The large relative error, $\approx 36\%$, of the Gaussian curvature K_g estimated geometrically comes from the misalignments and positioning errors of the transmitter, the receiver, and the SPP adopted to generate the radio-vortex.

The topological charge value, $l = 1.4 \pm 0.4$, is compatible with the twist imposed by the SPP. It has been obtained from C_I by exploiting the position of the singularity. Here the main source of error is still the vertical position of the scan path from the singularity. In our setup, the actual position of the singularity appears more critical than the curvature measurements in order to determine the topological charge. By increasing l the relative detection accuracy of the topological charge (measured at the same intensity and vertical distance y_0) remains constant. In fact, despite that ϕ_G does not depend on l the phase ϕ_{LG} is proportional to l. This introduces the benefit that the phase ϕ_{LG} becomes more easily distinguishable from the overall phase function $\phi(x)$ for $l > 1$. However, the error of the topological charge σ_l, due to the uncertainty of the vertical position y_0, is still proportional to l, keeping the relative accuracy σ_l/l constant.

In practical applications, where the measure of several OAM states is required, the singularity position could be easily obtained from the curvature itself by sending a known initial OAM reference state. On the contrary, the distance of the scanning line from the singularity is not strictly necessary for the local detection of OAM radiation. The Gaussian beam ($l = 0$) is distinguishable from a radio-vortex ($l \neq 0$) by checking the condition of the minimal surface $H_h \approx 0$, the negative sign of the Gaussian curvature or the inversion of the sign in C_I [11]. These quantities are directly obtained from the phase profiles.

Notice that when the position of the scanning line from the singularity is known, the curvature can also be measured by accessing a small portion of the scan. Obviously, despite that the locality of the proposed method is not limited in principle, the instrumental signal-to-noise-ratio should be increased by reducing the scan path, with the phase variation along the path being smaller.

REFERENCES

1. Bazhenov, V. Yu., M. V. Vasnetsov, and M. S. Soskin, "Laser beams with screw dislocations in their wavefronts," *JEPT Lett.*, Vol. 52, 429, 1990.
2. Bazhenov, V. Yu., M. S. Soskin, and M. V. Vasnetsov, "Screw dislocations in light wavefronts," *J. Mod. Optics*, Vol. 39, 985–990, 1992.
3. Allen, L., M. W. Beijersbergen, R. J. C. Spreeuw, and J. P. Woerdman, "Orbital angular momentum of light and the transformation of Laguerre-Gaussian laser modes," *Phys. Rev. A*, Vol. 45, 8185, 1992.

4. Yan, Y., et al., "High-capacity millimetre-wave communications with orbital angular momentum multiplexing," *Nature Communications*, Vol. 5, 4876, 2014.

5. Zhang, C. and L. Ma, "Detecting the orbital angular momentum of electro-magnetic waves using virtual rotational antenna," *Sci. Rep.*, Vol. 7, 4585, 2017.

6. Ren, Y., G. Xie, H. Huang, C. Bao, Y. Yan, N. Ahmed, M. P. J. Lavery, B. I. Erkmen, S. Dolinar, M. Tur, M. A. Neifeld, M. J. Padgett, R. W. Boyd, J. H. Shapiro, A. E. Willner, "Adaptive optics compensation of multiple orbital angular momentum beams propagating through emulated atmospheric turbulence," *Opt. Lett.*, Vol. 39, 2845, 2014.

7. Li, S., S. Chen, C. Gao, A. E. Willner, and J. Wang, "Atmospheric turbulence compensation in orbital angular momentum communications: Advances and perspectives," *Opt. Commun.*, Vol. 408, 68–81, 2018.

8. Paroli, B., E. Chiadroni, M. Ferrario, V. Petrillo, M. A. C. Potenza, A. R. Rossi, L. Serafini, and V. Shpakov, "Asymmetric lateral coherence of betatron radiation emitted in laser-driven light sources," *Europhys. Lett.*, Vol. 111, 44003, 2015.

9. Paroli, B., E. Chiadroni, M. Ferrario, A. Mostacci, V. Petrillo, M. A. C. Potenza, A. R. Rossi, and L. Serafini, "Coherence properties and diagnostics of betatron radiation emitted by an externally-injected electron beam propagating in a plasma channel," *Nucl. Instrum. Meth. Phys. Res. B*, Vol. 355, 217–220, 2015.

10. Paroli, B., E. Chiadroni, M. Ferrario, and M. A. C. Potenza, "Analogical optical modeling of the asymmetric lateral coherence of betatron radiation," *Opt. Express*, Vol. 23, 29912, 2015.

11. Paroli, B., M. Siano, and M. A. C. Potenza, "The local intrinsic curvature of wavefronts allows to detect optical vortices," *Opt. Express*, Vol. 27, 17550–17560, 2019.

12. Paroli, B., M. Siano, L. Teruzzi, and M. A. C. Potenza, "Single-shot measurement of phase and topological properties of orbital angular momentum radiation through asymmetric lateral coherence," *Phys. Rev. Acc. and Beams*, Vol. 22, 032901, 2019.

13. Paroli, B., A. Cirella, I. Drebot, V. Petrillo, M. Siano, and M. A. C. Potenza, "Asymmetric lateral coherence of OAM radiation reveals topological charge and local curvature," *J. Opt.*, Vol. 20, 075605, 2018.

14. Meusnier, J. B., "Mémoire sur la courbure des surfaces," *Mém. Mathém. Phys. Acad. Sci. Paris, prés. par div. Savans*, Vol. 10, 477–510, 1785 (Presented in 1776).

15. Schoen, R., "Uniqueness, symmetry, and embeddedness of minimal surfaces," *J. Differ. Geom.*, Vol. 18, 791–809, 1983.

16. Paroli, B., M. Siano, and M. A. C. Potenza, "Asymmetric lateral coherence allows precise wavefront characterization," *Europhys. Lett.*, Vol. 122, 44001, 2018.

17. Meeks, W. H. and J. P'erez, "The classical theory of minimal surfaces," *Bulletin (New Series) of the American Mathematical Society*, Vol. 48, 325–407, 2011.